UNIVERSITY OF BIRMINGHAM
University of Birmingham Research at Birmingham

Acoustic bubble dynamics in a microvessel surrounded by elastic material

Wang, SP; Wang, Qian; Leppinen, David; Zhang, A. M.; Liu, YL

DOI:
10.1063/1.5005534

License:
Other (please specify with Rights Statement)

Document Version
Publisher's PDF, also known as Version of record

Citation for published version (Harvard):
Wang, SP, Wang, Q, Leppinen, D, Zhang, AM & Liu, YL 2018, 'Acoustic bubble dynamics in a microvessel surrounded by elastic material', *Physics of Fluids*, vol. 30, no. 1, 012104. https://doi.org/10.1063/1.5005534

Link to publication on Research at Birmingham portal

Publisher Rights Statement:
Checked for eligibility: 28/10/2019

This article may be downloaded for personal use only. Any other use requires prior permission of the author and AIP Publishing. This article appeared in Wang, S.P., Wang, Q.X., Leppinen, D.M., Zhang, A.M. and Liu, Y.L., 2018. Acoustic bubble dynamics in a microvessel surrounded by elastic material. Physics of Fluids, 30(1), p.012104., and may be found at: https://doi.org/10.1063/1.5005534

General rights
Unless a licence is specified above, all rights (including copyright and moral rights) in this document are retained by the authors and/or the copyright holders. The express permission of the copyright holder must be obtained for any use of this material other than for purposes permitted by law.

•Users may freely distribute the URL that is used to identify this publication.
•Users may download and/or print one copy of the publication from the University of Birmingham research portal for the purpose of private study or non-commercial research.
•User may use extracts from the document in line with the concept of 'fair dealing' under the Copyright, Designs and Patents Act 1988 (?)
•Users may not further distribute the material nor use it for the purposes of commercial gain.

Where a licence is displayed above, please note the terms and conditions of the licence govern your use of this document.

When citing, please reference the published version.

Take down policy
While the University of Birmingham exercises care and attention in making items available there are rare occasions when an item has been uploaded in error or has been deemed to be commercially or otherwise sensitive.

If you believe that this is the case for this document, please contact UBIRA@lists.bham.ac.uk providing details and we will remove access to the work immediately and investigate.

Download date: 24. Apr. 2024

Physics of Fluids

Acoustic bubble dynamics in a microvessel surrounded by elastic material

Cite as: Phys. Fluids **30**, 012104 (2018); https://doi.org/10.1063/1.5005534
Submitted: 18 September 2017 . Accepted: 20 December 2017 . Published Online: 10 January 2018

S. P. Wang, Q. X. Wang, D. M. Leppinen, A. M. Zhang, and Y. L. Liu

View Online Export Citation CrossMark

ARTICLES YOU MAY BE INTERESTED IN

Experimental and numerical study on bubble-sphere interaction near a rigid wall
Physics of Fluids **29**, 092102 (2017); https://doi.org/10.1063/1.4993800

Oscillation of a bubble in a liquid confined in an elastic solid
Physics of Fluids **29**, 072101 (2017); https://doi.org/10.1063/1.4990837

Experimental and numerical study of the effects of a wall on the coalescence and collapse of bubble pairs
Physics of Fluids **30**, 042107 (2018); https://doi.org/10.1063/1.5024946

AIP Publishing

© 2018 Author(s).

Acoustic bubble dynamics in a microvessel surrounded by elastic material

S. P. Wang,[1] Q. X. Wang,[2,3,a)] D. M. Leppinen,[2] A. M. Zhang,[1] and Y. L. Liu[1]
[1]*College of Shipbuilding Engineering, Harbin Engineering University, Harbin 150001, Heilongjiang, People's Republic of China*
[2]*School of Mathematics, University of Birmingham, Birmingham B15 2TT, United Kingdom*
[3]*School of Naval Architecture, Dalian University of Technology, Dalian 116024, China*

(Received 18 September 2017; accepted 20 December 2017; published online 10 January 2018)

This paper is concerned with microbubble dynamics in a blood vessel surrounded by elastic tissue subject to ultrasound, which are associated with important applications in medical ultrasonics. Both the blood flow inside the vessel and the tissue flow external to the vessel are modeled using the potential flow theory coupled with the boundary element method. The elasticity of tissue is modeled through the inclusion of a pressure term in the dynamic boundary condition at the interface between the two fluids. Weakly viscous effects are considered using viscous potential flow theory. The numerical model is validated by comparison with the theoretical results of the Rayleigh-Plesset equation for spherical bubbles, the numerical results for acoustic bubbles in an unbounded flow, and the experimental images for a spark generated bubble in a rigid circular cylinder. Numerical analyses are then performed for the bubble oscillation, jet formation and penetration through the bubble, and the deformation of the vessel wall in terms of the ultrasound amplitude and the vessel radius. *Published by AIP Publishing.*
https://doi.org/10.1063/1.5005534

I. INTRODUCTION

We are concerned with acoustic microbubble dynamics in a deformable vessel. The vessel wall is defined by the material interface between two fluids. This phenomenon is associated with important applications in medical ultrasonics. Microbubbles are injected into the blood stream as a contrast agent for ultrasound imaging. The high compressibility of microbubbles compared to the surrounding tissue enables visualization of blood vessels down to the capillary level, and microbubbles are thus widely used in clinical diagnostic ultrasound.[1–5] Despite their clinical benefits, the potential damaging effects of microbubbles oscillating in close proximity to blood vessel walls remain a concern.[6–8]

This phenomenon is associated with bubbles in fluid-filled vessels (xylem) of plants, whose function is to transport the water and minerals from the roots to their leaves. Water shortage can introduce air bubbles into xylem, and the growth of bubbles in xylem is a cause of mortality during drought.[9] Acoustic emissions of pressure waves are associated with cavitation in plant xylem, and their applications in plant sciences are rapidly increasing, especially to investigate drought-induced plant stress.[10–13]

Klaseboer and Khoo[14] and Turangan *et al.*[15] presented a physical and numerical model to describe the behavior of an oscillating bubble in a fluid near a second elastic (biological) fluid, where the interface is assumed to be approximately a plane. The elasticity of the second fluid is modeled through a pressure term at the interface between the two fluids. The boundary element method (BEM) was then used to solve for the unknown normal velocities at both the bubble interface and fluid–fluid interface. Brujan *et al.*[16] carried out experiments for laser generated bubble dynamics near elastic gel and observed mushroom shaped bubbles. Curtiss *et al.*[17] simulated toroidal bubble dynamics near the interface of two liquids. Lind and Phillips[18,19] modeled the influence of viscoelasticity on the collapse of a bubble near a rigid and a free surface. Chen *et al.*[7] observed that ultrasound bubbles in microscopic blood vessels of rat mesentery are often associated with nonspherical deformation and liquid jetting.

The BEM is a grid-free method in the flow domain and has been widely used in bubble dynamics. Calvisi *et al.*[20] and Fong *et al.*[21,22] simulated acoustic bubble dynamics using the potential flow theory and BEM for an axisymmetric configuration. Wang and Blake[23,24] modeled the compressible effects of the liquid flow surrounding the bubble by developing the weakly compressible theory. Wang and Manmi[25,26] implemented a three-dimensional BEM model for bubble dynamics near a rigid boundary subject to acoustic waves traveling parallel to the boundary.

In this paper, acoustic microbubble dynamics in a deformable vessel are modeled following the physical model of Refs. 14, 15, and 27. Both the blood flow inside the vessel and the tissue flow external to the vessel are modeled using the incompressible potential flow theory coupled with the BEM. The two fluids can have different densities, and the fluid outside the elastic vessel is assumed to be associated with elasticity.

In the present work, the viscous effects are approximately modeled using the viscous potential flow theory. Viscous fluid dynamics can be approximately described by the viscous potential flow theory when the vorticity is small or is confined to a narrow layer near the boundary.[28,29] It is particularly useful for a gas–liquid two-phase flow with an interface. A key

[a)]Author to whom correspondence should be addressed: q.x.wang@bham.ac.uk

issue in the theory is that the shear stress should vanish approximately at a gas–liquid interface, but it does not in the potential flow approximation. An auxiliary function, the viscous pressure correction to the potential pressure, has been introduced to address this discrepancy by Joseph and Wang.[30] This theory was applied for transient bubble dynamics based on the BEM by Klaseboer *et al.*,[31] Li *et al.*,[32] and Zhang and Ni[33] for a bubble rising and deforming in a viscous liquid and by Manmi and Wang for acoustic bubble dynamics.[34]

The numerical model is validated by comparison with the theoretical results of the Rayleigh-Plesset Equation (RPE) for spherical bubbles, the numerical results for acoustic bubbles in an unbounded flow, and the experimental images for spark generated bubbles in a rigid circular cylinder. Parametric studies are then performed for acoustic bubble dynamics in an elastic vessel and for the vessel wall deformation.

II. NUMERICAL MODEL

Suppose fluid 1 and fluid 2 have an interface S_i, which initially takes the shape of a circular cylinder, as illustrated in Fig. 1. Fluid 1, such as blood in which the bubble resides, is supposed to be a Newtonian fluid that has no elasticity. In general, the blood is non-Newtonian. Some non-Newtonian effects of liquids are modeled based on the potential flow theory.[19,35] Fluid 2 has some elastic properties. The densities of the two fluids can be different. Initially, a spherical bubble is at an equilibrium radius R_0 with its centre positioned at the centre of the configuration. The cylindrical coordinates (r, θ, z) are adopted with the origin at the centre of the configuration and the z-axis along the axis of symmetry. The initial radius of the vessel is R_D, and the length of the vessel is L. The deformation of the interface S_i from the undisturbed state along the radial direction is denoted as h. Although the real applications are often 3D cases, the asymmetrical cases studied are expected to provide the magnitude and trend of the phenomenon in terms of the frequency and amplitude, vessel radius, etc. The incident pressure wave along the z-axis is given as follows:

$$p_\infty(z,t) = p_\infty + a\sin(kz - \omega t), \tag{1}$$

where t is the time, p_∞ is the atmospheric pressure, a is the amplitude, k is the wavenumber, and ω is the angular frequency of the pressure wave.

We assume that both flows 1 and 2 are incompressible and potential.[37–39] The continuity equation for the two fluids implies

$$\nabla^2\phi_l = 0, \quad l = 1, 2, \tag{2}$$

where the subscript $l = 1, 2$ stands for fluids 1 and 2, respectively, and ϕ_l is the velocity potential. Note that the compressible effects are essential for very short periods at the end of collapse, which results in significant damping of oscillation from the first cycle to the second cycle of oscillation.[13,40,41] However, it does not significantly affect the pressure field.[32,36]

The Bernoulli equation in fluids 1 and 2 can be expressed as

$$\frac{\partial\phi_l}{\partial t} = \frac{p_\infty - p_l}{\rho_l} - \frac{1}{2}|\nabla\phi_l|^2, \quad l = 1, 2, \tag{3}$$

where ρ_l is the fluid density. The effects of buoyancy are neglected here since we are concerned with microbubbles.

The dynamic boundary condition on the bubble surface reads

$$p_{bub} - p_1 + 2\mu\frac{\partial^2\phi_1}{\partial n^2} = \sigma\kappa + p_{vc}, \tag{4}$$

where p_{bub} is the bubble internal pressure, p_1 is the fluid pressure outside the bubble, μ is the dynamic viscosity of fluid 1, σ is the surface tension, and κ is the curvature of the bubble surface. The viscous pressure correction, p_{vc}, is at the bubble surface and is introduced to compensate the non-zero shear stress of the potential flow at the bubble surface.[28,30,34] The viscous correction pressure p_{vc} is obtained using[33,34]

$$p_{vc} = -2\mu C\frac{\partial^2\phi_1}{\partial n^2}, \tag{5}$$

where the coefficient C is obtained through the relationship

$$\int_{S_b}\frac{\partial\phi_1}{\partial n}(-p_{vc})dS = \int_{S_b}\frac{\partial\phi_1}{\partial\tau}\tau_s dS, \tag{6}$$

where $\boldsymbol{\tau}$ and $\boldsymbol{n}$ are the tangential and normal vectors of the bubble surface, respectively, and S_b is the bubble surface.

Assuming that the bubble gas is under an adiabatic process, its pressure p_{bub} satisfies

$$p_{bub}(t) = p_{sat} + p_{g0}\left(\frac{V_0}{V}\right)^\gamma, \tag{7}$$

where p_{sat} is the saturated vapor pressure of fluid 1, p_{g0} is the initial pressure of the bubble gas, V_0 and V are the initial and transient bubble volumes, and γ is the specific heat ratio of the bubble gas. Fuster and Montel[42] showed that for very fast oscillations, the effective polytropic coefficient of the mixture recovers the adiabatic limit given that neither heat nor mass transfer has time to significantly modify the pressure inside the bubble. The thermal processes typically absorb a relatively small portion of the overall energy.[43] Heat and mass transfer across the bubble surface can be included in the model.[44]

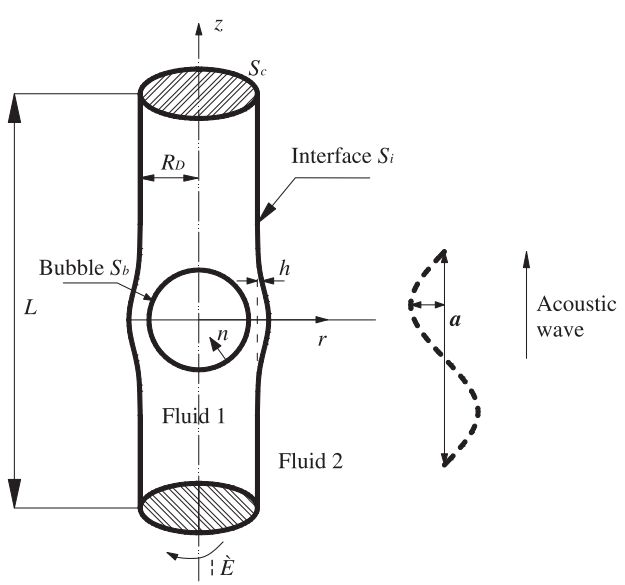

FIG. 1. Sketch of a bubble S_b pulsating in an elastic vessel S_i, with fluid 1 inside the vessel and fluid 2 outside the vessel, subject to an acoustic wave along the z-axis.

Using the Bernoulli equation, the dynamic boundary condition (3) on the bubble surface can be expressed as

$$\rho_1 \frac{d\phi_1}{dt} = \frac{1}{2}\rho_1 u^2 + p_\infty(z,t) + p_{vc} - p_0\left(\frac{V_0}{V}\right)^\gamma - 2\mu\frac{\partial^2\phi_1}{\partial n^2} + \sigma\kappa, \tag{8}$$

where both the surface tension and weakly viscous effects are considered.

The potentials of the two flows satisfying Laplace's equation can be expressed as

$$\lambda_1(\boldsymbol{r})\phi_1(\boldsymbol{r}) = \int_{S_b+S_i} \frac{1}{|\boldsymbol{r}-\boldsymbol{r}_s|}\frac{\partial\phi_1(\boldsymbol{r}_s)}{\partial n} - \phi_1(\boldsymbol{r}_s) \times \frac{\partial}{\partial n}\left(\frac{1}{|\boldsymbol{r}-\boldsymbol{r}_s|}\right) dS(\boldsymbol{r}_s) \quad \text{for fluid 1}, \tag{9}$$

$$\lambda_2(\boldsymbol{r})\phi_2(\boldsymbol{r}) = -\int_{S_b+S_i} \frac{1}{|\boldsymbol{r}-\boldsymbol{r}_s|}\frac{\partial\phi_2(\boldsymbol{r}_s)}{\partial n} - \phi_2(\boldsymbol{r}_s) \times \frac{\partial}{\partial n}\left(\frac{1}{|\boldsymbol{r}-\boldsymbol{r}_s|}\right) dS(\boldsymbol{r}_s) \quad \text{for fluid 2}, \tag{10}$$

where $\boldsymbol{r}$ and $\boldsymbol{r}_s$ are the field point and source point, respectively, and λ_1 and λ_2 are the solid angles at the field point on the boundary of the fluids 1 and 2, respectively. The normal directions in both (9) and (10) on the interface are external to fluid 1. The two solid angles satisfy $\lambda_1(\boldsymbol{r}) + \lambda_2(\boldsymbol{r}) = 4\pi$ at the interface.

The pressure difference between fluid 1 and fluid 2 at the interface S_i is assumed to be linearly dependent to the displacement h of the interface from its undisturbed position,[14]

$$p_1 = p_2 + Kh, \tag{11}$$

where $K \geq 0$ is the elastic parameter representing elasticity property of fluid 2 outside the vessel. When $K = 0$, the pressure across the interface is continuous and there is no elasticity in fluid 2. The normal velocity is continuous at the interface S_i.

Multiplying ρ_l on both sides of (3) and subtracting the resulting equation for fluid 1 and that for fluid 2, we have

$$\rho_2\frac{\partial\phi_2}{\partial t} - \rho_1\frac{\partial\phi_1}{\partial t} = p_1 - p_2 + \frac{1}{2}\rho_1|\nabla\phi_1|^2 - \frac{1}{2}\rho_2|\nabla\phi_2|^2.$$

Dividing the above equation by ρ_2 yields

$$\frac{\partial\phi_2}{\partial t} - \alpha\frac{\partial\phi_1}{\partial t} = \frac{-p_2+p_1}{\rho_2} - \frac{1}{2}\left(|\nabla\phi_2|^2 - \alpha|\nabla\phi_1|^2\right) \quad \text{on } Si, \tag{12}$$

where $\alpha = \rho_1/\rho_2$ is the density ratio of the two fluids.

Equation (12) can be written as[15]

$$\frac{D}{Dt}(\phi_2 - \alpha\phi_1) = \nabla\phi_1\cdot\nabla\phi_2 - \frac{1}{2}\left(|\nabla\phi_2|^2 + \alpha|\nabla\phi_1|^2\right) + \frac{Kh}{\rho_2} \quad \text{on } Si, \tag{13}$$

where $\frac{D}{Dt} = \frac{\partial}{\partial t} + \nabla\phi_1\cdot\nabla$ is the material derivative with respect to velocity $\nabla\phi_1$.

The reference length is chosen as the initial bubble radius R_0, the reference pressure is $\Delta p = p_\infty - p_{sat}$, and the density of fluid 1 is the reference density. Nondimensionalization is performed with the reference scales, and dimensionless variables will be noted with upper bars.

Equations (8) and (13) can be written in the dimensionless form as follows:

$$\frac{d\overline{\phi}_1}{d\overline{t}} = \frac{1}{2}\overline{u}^2 + 1 - \varepsilon\left(\frac{\overline{V}_0}{\overline{V}}\right)^\gamma - \frac{2(1+C)}{Re}\frac{\partial^2\overline{\phi}_1}{\partial n^2} + \frac{\kappa}{We} + \overline{a}\sin\left(\overline{k}\overline{z} - \overline{\omega}\overline{t}\right), \tag{14}$$

$$\frac{D}{D\overline{t}}\left(\overline{\phi}_{i2} - \alpha\overline{\phi}_{i1}\right) = \nabla\overline{\phi}_{i1}\cdot\nabla\overline{\phi}_{i2} - \frac{1}{2}\left(\left|\nabla\overline{\phi}_{i2}\right|^2 + \alpha\left|\nabla\overline{\phi}_{i1}\right|^2\right) + \overline{Kh}, \tag{15}$$

where $\varepsilon = p_{g0}/\Delta p$ is the strength parameter, $Re = (\Delta p\rho_1)^{0.5}R_0/\mu$ is the Reynolds number, $We = R_0\Delta p/\sigma$ is the Weber number, and $\overline{K} = 2\alpha K/(3\Delta p)$ is the elastic parameter for fluid 2.

The kinematic condition on both the bubble surface and the interface of two fluids can be expressed as

$$\frac{D\overline{\boldsymbol{r}}}{D\overline{t}} = \nabla\overline{\phi}. \tag{16}$$

A high-speed liquid jet often forms toward the end of the collapse of a nonspherical bubble, and it subsequently penetrates through the bubble. The liquid domain is then transformed from a singly connected to a doubly connected form, which results in non-unique solutions to the potential flow model. We adopt the vortex ring model by Wang *et al.*[41,45] and Liu *et al.*[46] to model the topological transition of a bubble and the subsequent toroidal bubble motion.

In the vortex ring model, a vortex ring is placed inside the toroidal bubble once the jet impacts on the opposite bubble surface. The circulation Γ of the vortex-ring is equal to the jump of the potential $\overline{\phi}$ across the contact point at the time of impact. The potential $\overline{\phi}$ is then decomposed as follows:

$$\overline{\phi} = \overline{\varphi}_{vr} + \overline{\varphi}, \tag{17}$$

where $\overline{\varphi}_{vr}$ is the potential due to the vortex ring which can be calculated using the Biot-Savart law[41,47] and $\overline{\varphi}$ is the remnant potential, which is continuous in the flow domain.

The dynamic boundary conditions on the bubble surface (14) and the interface (15) can be written in terms of the remnant potential $\overline{\varphi}$, respectively, as follows:

$$\frac{D\overline{\varphi}_1}{Dt} = 1 - \varepsilon\left(\frac{\overline{V}_0}{\overline{V}}\right)^\gamma + \frac{1}{2}|\nabla\overline{\varphi}_1 + \nabla\overline{\varphi}_{vr}|^2 - \nabla\overline{\varphi}_{vr}\cdot(\nabla\overline{\varphi}_{vr} + \nabla\overline{\varphi}_1) - \frac{2(1+C)}{Re}\frac{\partial^2\overline{\phi}_1}{\partial n^2} + \frac{\overline{\kappa}}{We} + \overline{a}\sin\left(\overline{k}\overline{z} - \overline{\omega}\overline{t}\right) \quad \text{on } S_b, \tag{18}$$

$$\frac{D}{Dt}(\overline{\varphi}_2 - \alpha\overline{\varphi}_1) = (\nabla\overline{\varphi}_1 + \nabla\overline{\varphi}_{vr})\cdot(\nabla\overline{\varphi}_2 - \alpha\nabla\overline{\varphi}_{vr}) + \frac{1}{2}\alpha|\nabla\overline{\varphi}_1 + \nabla\overline{\varphi}_{vr}|^2 - \frac{1}{2}|\nabla\overline{\varphi}_2 + \nabla\overline{\varphi}_{vr}|^2 + \overline{Kh} \quad \text{on } S_i. \tag{19}$$

At each time step, we have known bubble and interface surfaces and known potential distributions on them. With this information, we can calculate the tangential velocity on the two surfaces. The normal velocities on them are obtained by solving the boundary integral equations (9) and (10). The bubble and interface surfaces and the potential distributions on them can be further updated by performing the Lagrangian time integration to (14)–(16), respectively. The details on the

numerical model using the BEM for the problem can be found in Refs. 48–50.

We will discuss the calculation of the diagonal elements of the influence coefficient matrix. The boundary integral equations (9) and (10) are discretized using a linear representation of the potential and normal velocity. Integrating and storing the results for each node in a vector form will give rise to the following matrix equation:

$$H\phi = G\frac{\partial \phi}{\partial n}, \tag{20}$$

where G and H are the influence matrices.[47]

The calculation of the diagonal elements of the matrix H is often associated with singularities, and these can be eliminated for a closed surface using the relation $H_{ii} = -\sum_{\substack{j=1\\ j\neq i}}^{N} H_{ij}$, where N is the total number of nodes on the surface. This works fine for the closed bubble surface. However, the interface has to be truncated in the numerical modeling and has two open ends.

To resolve this problem, we close the two open ends of the interface using two auxiliary cross sections S_{c1} and S_{c2} of the vessel, as shown in Fig. 1, whose centers are located at $(0, L/2)$ and $(0, -L/2)$ with their normal vectors parallel to the z-axis. The influence of the two cross sections to a field point $\boldsymbol{r}$ can be expressed as

$$\begin{aligned}\beta_k(\boldsymbol{r}) &= \int_{S_c} \frac{(\boldsymbol{r}-\boldsymbol{r}_s)\cdot \boldsymbol{n}}{|\boldsymbol{r}-\boldsymbol{r}_s|^3} dS \\ &= (-1)^{k-1}\int_0^{2\pi} d\theta \int_0^{R_D} \\ &\quad \times \frac{z - z_k}{\left((x - r_s\sin\theta)^2 + (y - r_s\cos\theta)^2 + (z - z_k)\right)^{3/2}} r_s dr_s,\end{aligned} \tag{21}$$

where $k = 1, 2$, $z_1 = L/2$, and $z_2 = -L/2$ are associated with the two auxiliary cross sections, respectively.

The diagonal elements of the matrix H can thus be calculated accurately using the following formulae:

$$H_{ii} = -\sum_{\substack{j=1\\ j\neq i}}^{N} H_{ij} - \beta_1(\boldsymbol{r}_i) - \beta_2(\boldsymbol{r}_i). \tag{22}$$

III. VALIDATIONS OF THE NUMERICAL MODEL

A. Comparison with the Rayleigh-Plesset equation

We first compare the BEM computation with the Rayleigh-Plesset equation (RPE)[51] for the oscillation of a spherical bubble in an infinite fluid for $\varepsilon = 100$, $\gamma = 1.25$, $\overline{R}_0 = 1$, $\overline{p}_{sat} = 0$, and $Re = 100$ and 10, respectively, ignoring the surface tension effect. The RPE is integrated using the 4th order Runge-Kutta method. For this case, we have $\alpha = 1.0$, $\overline{K} = 0.0$, $\overline{a} = 0$, and $\overline{\omega} = 0$. As shown in Fig. 2, the BEM agrees accurately with the RPE over three cycles of oscillations. The bubble, which has a high initial pressure, expands and collapses in the medium, the maximum radius decreasing with time due to the viscous effect of the fluid. The damping of oscillation increases for a smaller Re.

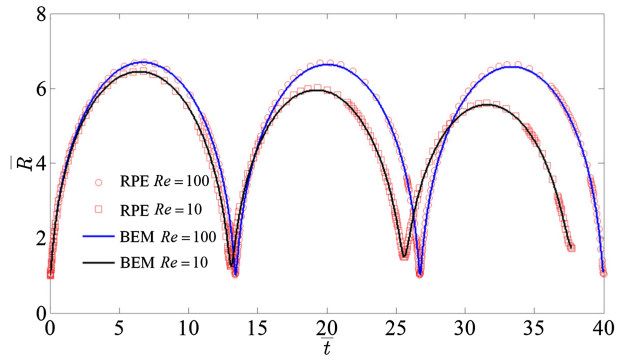

FIG. 2. Comparison between the BEM and RPE for the oscillation of a spherical bubble in an infinite fluid for $\varepsilon = 100$, $\overline{a} = 0$, $\overline{\omega} = 0$, $\gamma = 1.25$, $\alpha = 1$, $\overline{K} = 0$, $\overline{R}_D = 1.5$, $Re = 100$, and $\overline{p}_{sat} = 0$.

B. Comparison with computations for a bubble in an infinite flow

We compare the present model with that of Calvisi *et al.*[20] for a bubble subject to a traveling wave using the BEM. The case is characterized by $R_0 = 4.5\ \mu$m, $\omega = 1884$ kHz, $p_a = 1.6\Delta p$, $\gamma = 1.667$, $p_{sat} = 1837$ Pa, $p_\infty = 101\,000$ Pa, $\sigma = 0.0728$ N/m, and $\mu = 0$ Pa s. The corresponding dimensionless parameters are $\alpha = 1.0$, $\overline{K} = 0.0$, and $\overline{R}_D = 1.5$. Figure 3 shows the bubble shapes at the very moment when the bubble jet impacts on the opposite bubble surface at $\overline{t} = 5.53$. The results of the two models agree well for both the jet and bubble shapes. The solid line on both sides of the figure gives the position of an artificial fluid interface initially positioned at $\overline{R}_D = 1.5$.

C. Comparison with experiments

To further validate the present numerical model, we carry out experiments to observe the dynamics of a bubble in a solid tube in a cubic glass tank with 0.5 m side length filled with water. An electronic spark[53,54] is used to generate a bubble at the centre of a rigid circular cylinder.

In the experiments, the ambient pressure is 998 kPa, the room temperature is 20 °C, the water density is 998 kg/m^3,

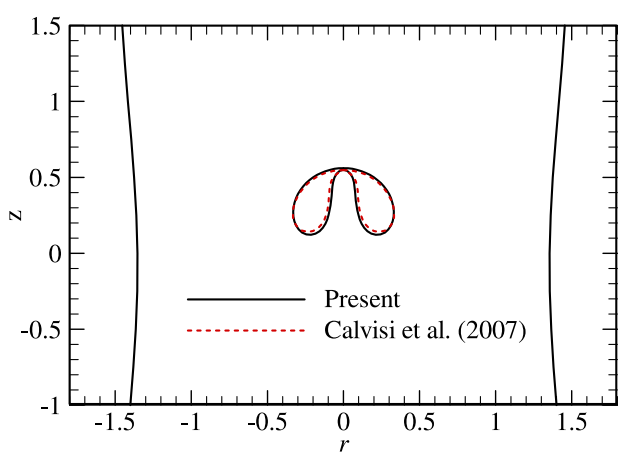

FIG. 3. Comparison between the present model and that of Calvisi *et al.*[20] for a bubble subject to an acoustic wave at $\overline{t} = 5.53$. The parameters used are $\varepsilon = 1.3252$, $\overline{a} = 1.6$, $\overline{\omega} = 0.8496$, $\overline{k} = 0.0057$, $\gamma = 1.667$, $\alpha = 1$, $\overline{K} = 0$, $We = 6.15$, $\overline{R}_D = 1.5$, $Re = 0$, and $\overline{p}_{sat} = 0.018$.

the dynamic viscous coefficient is 0.001 Pa s, and the surface tension is 0.0728 N/m. The parameter ε is chosen as 100, and the corresponding maximum radius $\overline{R}_m = 6.1$ is determined from[52]

$$\varepsilon = \frac{\left(1 - \overline{R}_m^3\right)(1-\gamma)}{1 - \overline{R}_m^{3(1-\gamma)}}, \tag{23}$$

which is obtained from the Rayleigh-Plesset equation. The choice of the strength parameter does not affect numerical results significantly.[15,52]

The inner radius of the cylinder is $R_D = 17.5$ mm, the maximum bubble radius is 14.6 mm, and the initial radius is $R_0 = 2.4$ mm. The corresponding dimensionless inner vessel radius $\overline{R}_D = 7.3$, the Reynolds number $Re = 7.6 \times 10^4$, and the Weber number $We = 3.3 \times 10^4$. A bubble collapsing in a rigid circular cylinder corresponds with the density of fluid 2 being infinite i.e., $\alpha \to 0$. In the numerical simulations, $\alpha = 0.001$ and $\overline{K} = 0$ are chosen for a rigid circular cylinder.

The experimental and numerical results are compared in Fig. 4. The snapshots in the figure are at the same "time" for both model and experiments. The bubble expands from Figs. 4(a) and 4(b) reaching its maximum volume at $t = 4.48$ ms [Fig. 4(b)]. It then collapses, with the two ends becoming flattened during the early stage of collapse [Fig. 4(c)]; two inward jets along the axis of symmetry form subsequently [Fig. 4(d)]. The two counter jets penetrate the bubble and subsequently collide with each other [Fig. 4(e)]. The impact of

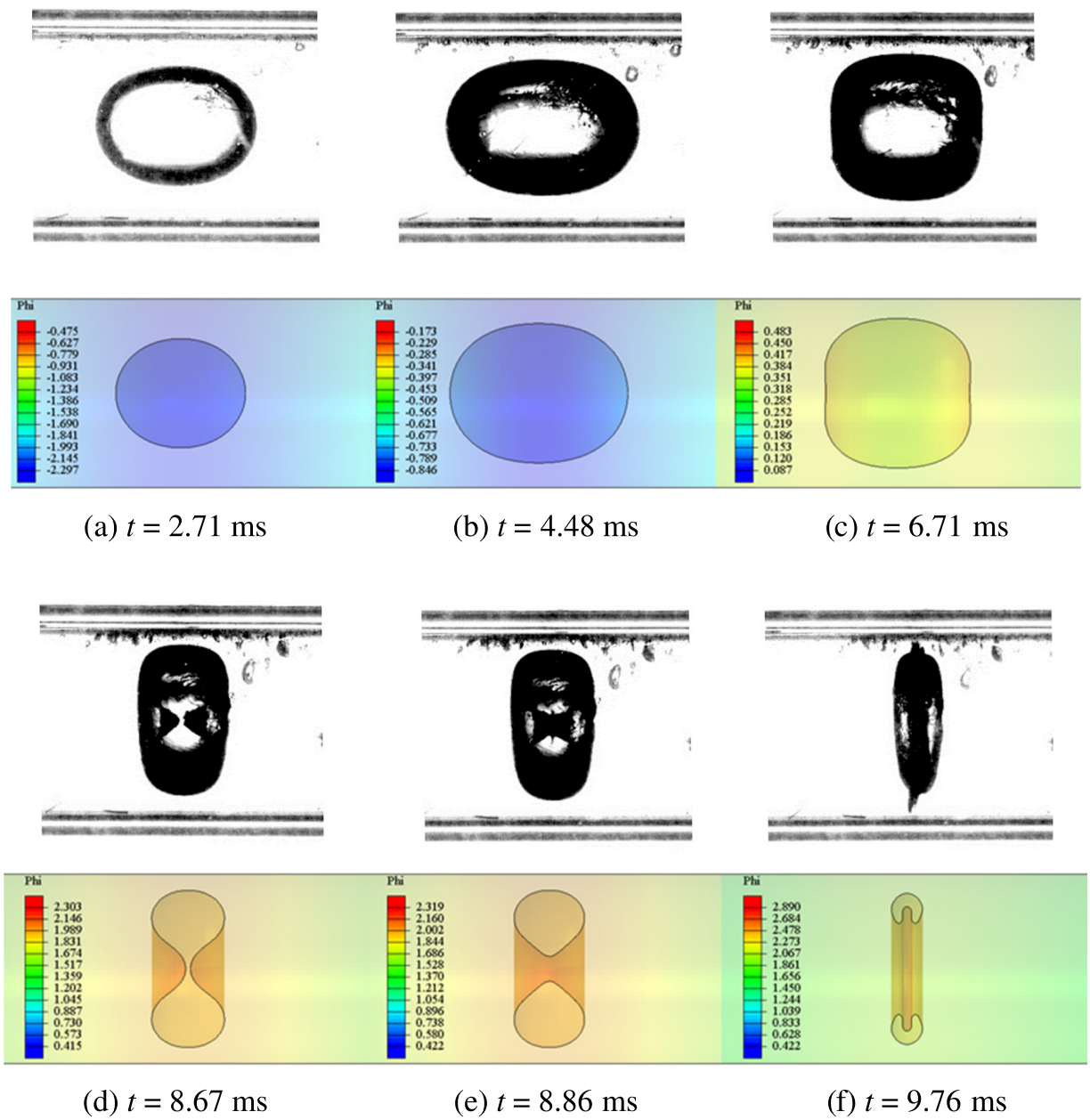

(a) $t = 2.71$ ms (b) $t = 4.48$ ms (c) $t = 6.71$ ms

(d) $t = 8.67$ ms (e) $t = 8.86$ ms (f) $t = 9.76$ ms

FIG. 4. Comparison between the experiments and BEM computations for the dynamics of a spark generated bubble for the vessel's inner radius 17.5 mm, maximum bubble radius 14.6 mm, and $\varepsilon = 100$, $\overline{R}_0 = 1$, $\overline{R}_D = 1.2$, $Re = 2.2 \times 10^4$, $We = 3.0 \times 10^3$, $\alpha = 0.001$, and $\overline{K} = 0$, for (a) $t = 2.71$ ms, (b) $t = 4.48$ ms, (c) $t = 6.71$ ms, (d) $t = 8.67$ ms, (e) $t = 8.86$ ms, and (f) $t = 9.76$ ms.

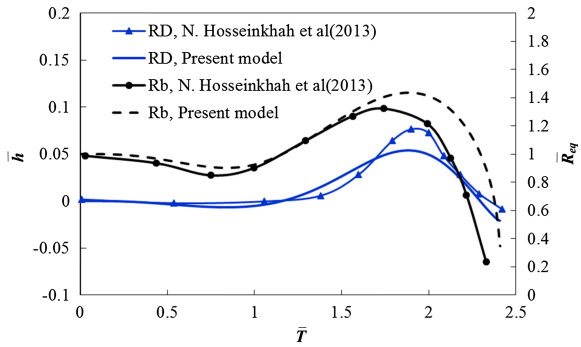

FIG. 5. The comparison of the present calculation with the experiments[55] for the time histories of the dimensionless equivalent bubble radius $\overline{R}_{eq}$ and the dimensionless deformation $\overline{h}$ of the elastic vessel wall at the mid-cross section. The parameters used are $\varepsilon = 1$, $\gamma = 1.07$, $\alpha = 1$, $\overline{K} = 0.32$, $We = 4.36$, $\overline{R}_D = 5.33$, $Re = 30.71$, and $\overline{p}_{sat} = 0$.

the two counter jets results in a ring jet as the bubble further collapses, as shown in Fig. 4(f).

D. Comparison with experiments for bubble dynamics in microvessel

To further validate the present numerical model, we compare with the experiments[54] for bubble dynamics at the center of an elastic microvessel driven by an ultrasound wave. The experimental case is characterized by $R_0 = 4.7$ μm, $R_D = 21$ μm, $\gamma = 1.07$, $p_{sat} = 0$ Pa, $p_\infty = 104.6$ kPa, $K = 50$ kPa, $\sigma = 0.072$ N/m, and $\mu = 0.001$ Pa s. The ultrasound wave applied is with a peak negative pressure of 0.8 MPa and frequency 1 MHz. The corresponding dimensionless parameters are calculated as $\varepsilon = 1$, $\alpha = 1$, $\overline{K} = 0.32$, $We = 4.36$, $\overline{R}_D = 5.33$, and $Re = 30.71$.

Figure 5 shows the comparison of the present calculation with the experiments for the time histories of the dimensionless equivalent bubble radius $\overline{R}_{eq} = \sqrt[3]{3V/4\pi}$ and the dimensionless deformation $\overline{h}$ of the elastic vessel wall at the mid-cross section. In both of the computation and experiments, the bubble first collapses slightly before about $\bar{t} = 0.7$, then expands significantly, and subsequently re-collapses rapidly at much larger amplitude after reaching the maximum volume. In the meantime, the vessel wall is first pulled in slightly, then pushed away significantly, and afterwards pulled back again at much larger amplitude. The numerical results correlate well with the experimental data in terms of the trend and magnitude the bubble radius oscillation and vessel deformation.

IV. ULTRASONIC BUBBLE DYNAMICS IN AN ELASTIC MICROVESSEL

Brujan *et al.*[16] investigated a laser generated bubble collapsing near an elastic boundary, which consists of a transparent polyacrylamide (PAA) gel. The parameter K is the elastic property of the biological tissue, and it varies with different tissues. The parameter K has been tested through experiments, such as thoracic aorta with the elastic modulus K in the range of 0.04-0.9 MPa, articular cartilage (0.4-0.85 MPa), muscle (0.06-0.8 MPa), and cornea (0.3-5 MPa).[16] A range of the K-values is quoted here for each tissue type because the elastic modulus of biological tissues depends strongly on the applied stress. Microvessels are associated with inner diameters R_D smaller than 250 μm.[56] They can be divided into three groups in terms of diameters d: arterioles (250 μm $> d \geq 8$ μm), capillaries ($d < 8$ μm), and venules (250 μm $> d \geq 8$ μm).

We choose the elastic modulus $K = 0.405$ MPa, which is within the range of the elastic modulus of biological tissues. A bubble having the initial radius $R_0 = 4$ μm and saturated vapor pressure $p_{sat} = 1837$ Pa is at the equilibrium state before the arrival of the acoustic wave. Other parameters chosen are the hydrostatic pressure $p_{atm} = 998$ kPa, the specific heat ratio $\gamma = 1.4$, the elastic parameter $\overline{K} = 2.51$, and the density ratio $\alpha = 0.93$. The corresponding Weber number is $We = 5.5$ and the Reynolds number $Re = 40$. The bubble dynamics are analyzed in terms of the amplitude of ultrasound $\overline{a} = 0.1$, 1.0, 4.0, and 8.0.

The ultrasound is set at the natural frequency of the bubble, when the bubble is usually associated with strongest responses.[29,57] The natural frequency ω_n of a spherical gas bubble is given by[29]

$$\omega_n = \frac{1}{R_0}\sqrt{\frac{1}{\rho_1}\left(3\gamma\Delta P + 2\left(3\gamma - 1\right)\frac{\sigma}{R_0}\right)}. \tag{24}$$

For the parameters chosen above, we have $\omega_n = 0.9$ MHz or $\overline{\omega}_n = 2.32$ in dimensionless value.

A. Case for weak acoustic wave at amplitude $\overline{a} = 0.1$

We first consider the case for a weak pressure wave at amplitude $\overline{a} = 0.1$. Figure 6 shows the time history of the dimensionless bubble volume, $3\overline{V}/(4\pi)$, versus the history of the acoustic pressure at the centre of the initial bubble surface. The bubble starts expanding initially since the acoustic pressure is initially zero and decreases with time as $\bar{t} \leq \overline{T}_a/4$, where $\overline{T}_a$ is the period of the acoustic wave. It oscillates out of phase with the pressure wave. The oscillation becomes stable after about 15 cycles of oscillation.

Figures 7(a) and 7(b) display the bubble shape, velocity field (left), and pressure contour (right) at $\bar{t}/\overline{T}_a = 22.29$ and 22.82, when the bubble is at its maximum and minimum volumes, respectively. The bubble has oscillated for 22 cycles at the times considered but is still approximately spherical, as it

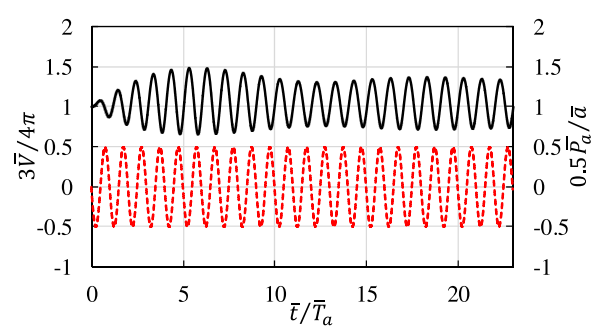

FIG. 6. Time history of the dimensionless bubble volume $3\overline{V}/(4\pi)$ for a bubble at the centre of an elastic vessel (solid line) for the dimensionless amplitude of ultrasound $\overline{a} = 0.1$ and vessel radius $\overline{R}_D = 1.5$, together with the time history of the pressure wave at the centre of the initial bubble surface. The remaining parameters are $R_0 = 4$ μm, $p_\infty = 998$ kPa, $\gamma = 1.4$, $\overline{K} = 2.51$, $\overline{\alpha} = 0.93$, $We = 5.5$, $Re = 40$, and $\overline{\omega} = 2.32$.

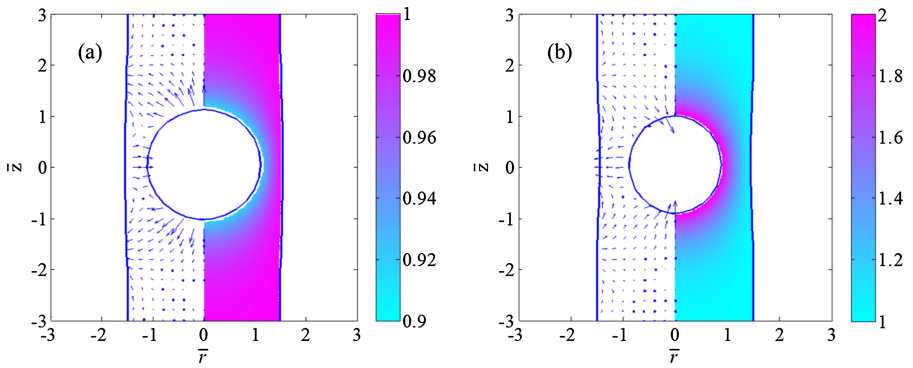

FIG. 7. Bubble shape, velocity field (left), and pressure contour (right) at (a) $\bar{t}/\bar{T}_a$ = 22.29 when the bubble is at its maximum volume and (b) $\bar{t}/\bar{T}_a$ = 22.82 when the bubble is at its minimum volume for the case in Fig. 6.

is subject to the weak pressure wave. At the maximum bubble volume [Fig. 7(a)], the elastic vessel wall presses the fluid between the bubble and elastic vessel wall inwards. As a result, the bubble surface near the elastic vessel wall begins to contract while the upper and lower parts of the bubble surface still expand outwards. In contrast, at the minimum bubble volume [Fig. 7(b)], the elastic vessel wall pulls the fluid between the bubble and elastic vessel wall outwards; the bubble surface near the elastic vessel wall begins to expand while the upper and lower parts of the bubble surface still collapse.

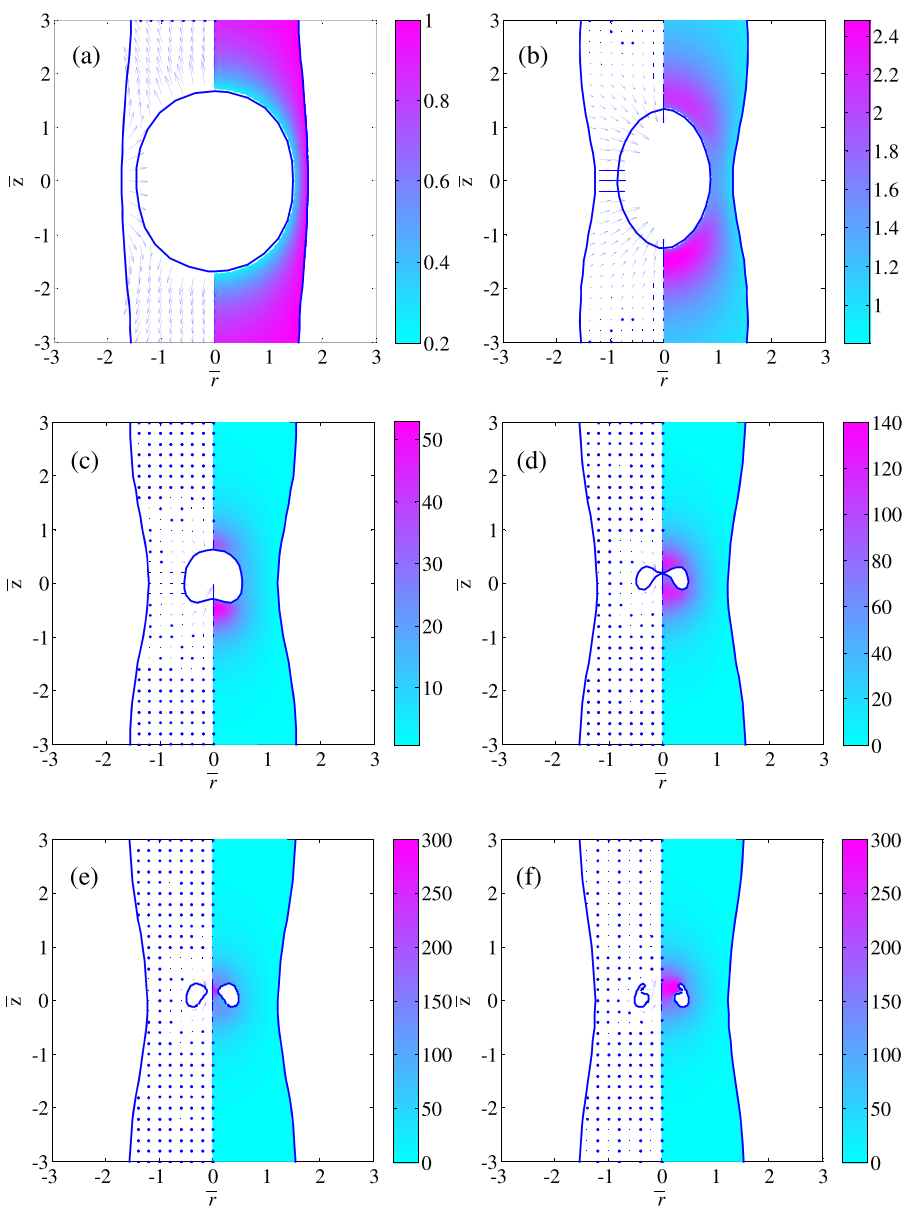

FIG. 8. Bubble shape, velocity field (left), and pressure counter (right) at $\bar{t}/\bar{T}_a$ = 0.585 (a), 0.838 (b), 0.887 (c), 0.897 (d), 0.898 (e), and 0.903 (f), for the acoustic wave amplitude $\bar{a} = 2.0$. The remaining parameters are the same as in Fig. 6.

B. Case for strong acoustic wave at amplitude $\bar{a}$ = 2

We then consider a case with strong ultrasound for $\bar{a} = 2$, with the remaining parameters being the same as in Fig. 6. The bubble oscillates with much larger amplitude and becomes nonspherical during the first cycle, as shown in Fig. 8. It becomes elongated along the vessel at its maximum volume due to the constraining effect of the vessel wall during the later stage of expansion [Fig. 8(a)]; at the same time, the vessel wall near the bubble is pushed outwards by the expanding bubble. The part of the bubble surface near the vessel wall compressed by the wall collapses while the top and bottom of the bubble surface expand. The side bubble surface then collapses faster than the top and bottom of the bubble surface; the elastic vessel is pulled back by the collapsing bubble forming a neck, and consequently the bubble becomes more elongate [Fig. 8(b)].

Two high fluid pressure zones form near the top and bottom of the bubble surface, with the lower one with the higher pressure of about 50 Δp. The two high pressure zones drive an upward liquid jet [Fig. 8(c)] and a downward jet [Fig. 8(d)], respectively. Recall that the acoustic wave is along the direction of the z-axis. The jet at the bottom of the bubble surface along the wave direction is stronger. The two jets impact each other [Fig. 8(d)], and the bubble collapses in a toroidal form subsequently [Figs. 8(d)–8(f)]. A high pressure zone results from the impact of the counter jets, which subsequently generates an annular jet pointing to the vessel wall [Fig. 8(f)].

C. Bubble volume and jet velocity

Figure 9(a) shows the bubble volume history subject to ultrasound at the amplitude $\bar{a} = 4$ in the elastic vessel with various radii $\bar{R}_D = 1.5$, 2, 3, 5, and 10, respectively. The remaining parameters are the same as in Fig. 6. The amplitude and period of oscillation increase with the vessel radius. The bubble reaches its dimensionless maximum volume 8.90 at $\bar{t}/\bar{T}_a = 0.63$ for $\bar{R}_D = 1.5$ and 12.66 at $\bar{t}/\bar{T}_a = 0.70$ for $\bar{R}_D = 10$.

Figure 9(b) shows the volume history of the bubble in the elastic vessel with a radius $\bar{R}_D = 1.5$ subject to ultrasound with various amplitudes $\bar{a} = 0.1$, 1.0, 2.0, 4.0, and 8.0, respectively. The amplitude and period of oscillation increase with the amplitude of ultrasound. The dimensionless bubble maximum and minimum volumes are 1.07 and 0.87, respectively, for $\bar{a} = 0.1$ when the bubble oscillates spherically (Figs. 6 and 7). The dimensionless bubble maximum and minimum volumes reach up to 24.0 and 0.007, respectively, for $\bar{a} = 8.0$, when the bubble oscillates nonspherically with jetting.

Figure 10 shows the time history of the jet velocity for the bubble subject to ultrasound at the amplitude $\bar{a} = 4$ in the elastic vessel with various radii $\bar{R}_D = 1.5$, 2, 3, 5, and 10, respectively. The jet velocity at the end of collapse is highest at $\bar{R}_D = 1.5$, being about 100 (1000 m/s in the dimensional form). It first reduces with $\bar{R}_D$ and then increases with $\bar{R}_D$ reaching its negative peak value at about $\bar{R}_D = 3$.

D. Deformation of vessel wall

We then consider the deformation of the elastic vessel wall. As shown in Figs. 8 and 9, the vessel wall is pushed away by an expanding bubble and is pulled back by a collapsing bubble. Figure 11(a) displays the time history of the deformation of the vessel wall at the middle cross section for different radii of the vessel $\bar{R}_D = 1.5$, 2, 3, 5, and 10, respectively, with the amplitude of ultrasound fixed at $\bar{a} = 4$. As expected, the vessel deformation is larger at a smaller radius $\bar{R}_D$. The elastic vessel at $\bar{R}_D = 1.5$ is pushed away with the maximum outward displacement $\bar{h} = 0.54$ at $\bar{t}/\bar{T}_a = 0.55$ before the bubble reaches its maximum volume at $\bar{t}/\bar{T}_a = 0.63$. It is pulled back with the largest inward displacement $\bar{h} = -0.53$ at $\bar{t}/\bar{T}_a = 0.91$ before the bubble reaches its minimum volume at $\bar{t}/\bar{T}_a = 0.92$.

Figure 11(b) shows the time history of the deformation of the elastic vessel wall at the middle cross section for

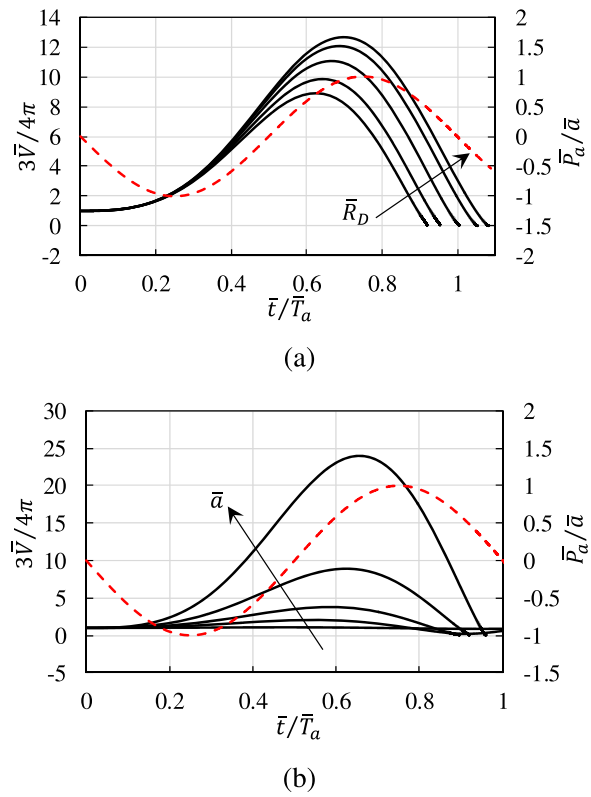

FIG. 9. Time history of bubble equivalent volume $3\bar{V}/(4\pi)$ for (a) acoustic wave amplitude $\bar{a} = 4$ and elastic vessel radii $\bar{R}_D = 1.5$, 2, 3, 5, and 10, respectively, and (b) $\bar{a} = 0.1$, 1.0, 2.0, 4.0, and 8.0, respectively, and $\bar{R}_D = 1.5$. The remaining parameters are the same as in Fig. 6. The dashed line displays the time history of the acoustic pressure at the centre of the initial bubble surface.

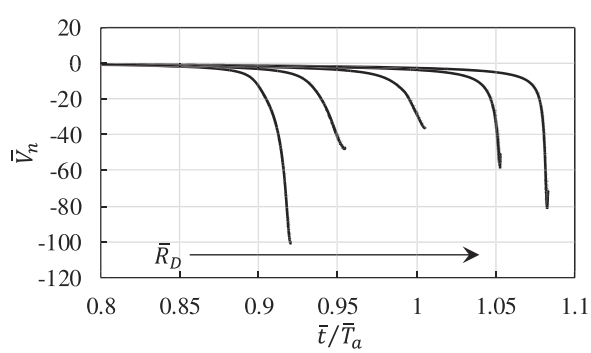

FIG. 10. Time histories of the jet velocity for $\bar{R}_D = 1.5$, 2, 3, 5, 10 and $\bar{a} = 4$. The remaining parameters are the same as in Fig. 6.

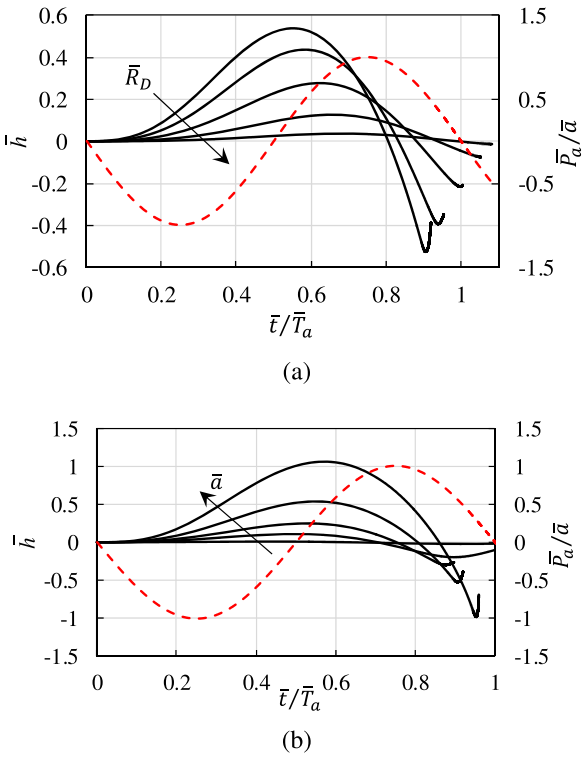

FIG. 11. Time histories of the deformation of the elastic vessel wall at the mid-cross section for (a) $\bar{R}_D$ = 1.5, 2, 3, 5, 10 and $\bar{a}$ = 4, and (b) $\bar{a}$ = 0.1, 1, 2, 4, 8 and $\bar{R}_D$ = 1.5. The remaining parameters are the same as in Fig. 6.

different amplitudes of the ultrasound $\bar{a}$ = 0.1, 1, 2, 4, and 8, respectively, with the radius of the elastic vessel fixed at $\bar{R}_D$ = 1.5. The deformation of the vessel wall increases significantly with $\bar{a}$. For $\bar{a}$ = 8.0, the vessel wall is pushed away to the largest outward displacement at $\bar{h}$ = 1.06 at $\bar{t}/\bar{T}_a$ = 0.57 before the bubble reaches its maximum volume at $\bar{t}/\bar{T}_a$ = 0.66 and pulled back to the largest inward displacement at $\bar{h}$ = −0.98 at $\bar{t}/\bar{T}_a$ = 0.95 before the bubble reaches its minimum volume at $\bar{t}/\bar{T}_a$ = 0.96.

V. CONCLUSIONS

We describe a numerical model to simulate microbubble dynamics in an elastic microvessel driven by an ultrasound wave, using the viscous potential flow theory coupled with the boundary element method. The elasticity of tissue is modeled through the addition of a pressure term in the dynamic boundary condition at the interface between the two fluids inside and outside of the vessel, respectively. The numerical model is validated by comparison with the Rayleigh-Plesset equation for spherical bubbles, the computations for nonspherical acoustic bubbles in an unbounded fluid, and the experiments for spark generated bubbles in a rigid circular cylinder. We further investigate microbubble dynamics in an elastic microvessel subject to ultrasound. The bubble expansion, collapse and topological transition, bubble jetting, and the deformation of the elastic vessel wall are analyzed with the following conclusions.

The bubble oscillates inside the vessel under ultrasound with different amplitudes. When the radius of the bubble and the vessel is of the same order, the bubble becomes elongated along the vessel subject to strong ultrasound due to the constraint of the elastic vessel wall. Two counter jets form along the axis of the vessel toward the end of the collapse. The jet along the direction of the acoustic wave forms earlier and with higher velocity. The impact of the two jets results in a ring jet pointing toward the vessel wall.

The elastic vessel wall is pushed outwards as the bubble expands and pulled inwards as it collapses. This "push" and "pull" phenomenon and associated oscillating normal deformation of the interface and the oscillating pressure difference across the interface are expected to enhance the membrane permeability for drug delivery. The expansion (contraction) of the vessel wall ceases before the bubble reaches its maximum (minimum) volume due to the elasticity of tissue outside the vessel. The deformation amplitude of the vessel wall increases with the amplitude of ultrasound and decreases with the radius of the vessel.

ACKNOWLEDGMENTS

This work was supported partially by the National Natural Science Foundation of China (Grant Nos. 11672082 and 51609044) and supported by EPSRC Grant No. EP/P015743/1.

[1] S. Dindyal and C. Kyriakides, "Ultrasound microbubble contrast and current clinical applications," Recent Pat. Cardiovasc. Drug Discovery **6**(1), 27–41 (2011).
[2] N. A. Hosny, G. Mohamedi, P. Rademeyer, J. Owen, Y. Wu, M. X. Tang, R. J. Eckersley, E. Stride, and M. K. Kuimova, "Mapping microbubble viscosity using fluorescence lifetime imaging of molecular rotors," Proc. Natl. Acad. Sci. U. S. A. **110**(23), 9225–9230 (2013).
[3] Q. X. Wang, W. K. Liu, A. M. Zhang, and Y. Sui, "Bubble dynamics in a compressible liquid in contact with a rigid boundary," Interface Focus **5**(5), 20150048 (2015).
[4] Y. Zhang, Y. Zhang, and S. Li, "Combination and simultaneous resonances of gas bubbles oscillating in liquids under dual-frequency acoustic excitation," Ultrason. Sonochem. **35**, 431–439 (2017).
[5] P. Prentice, A. Cuschieri, K. Dholakia, M. Prausnitz, and P. Campbell, "Membrane disruption by optically controlled microbubble cavitation," Nat. Phys. **1**(2), 107 (2005).
[6] D. L. Miller and J. Quddus, "Diagnostic ultrasound activation of contrast agent gas bodies induces capillary rupture in mice," Proc. Natl. Acad. Sci. U. S. A. **97**(18), 10179–10184 (2000).
[7] H. Chen, W. Kreider, A. A. Brayman, M. R. Bailey, and T. J. Matula, "Blood vessel deformations on microsecond time scales by ultrasonic cavitation," Phys. Rev. Lett. **106**, 034301 (2011).
[8] W. Wiedemair, Z. Tukovic, H. Jasak, D. Poulikakos, and V. Kurtcuoglu, "The breakup of intravascular microbubbles and its impact on the endothelium," Biomech. Model. Mechanobiol. **16**(2), 611–624 (2017).
[9] H. Cochard, "Cavitation in trees," C. R. Phys. **7**(9), 1018–1026 (2006).
[10] O. Vincent, P. Marmottant, S. R. Gonzalez-Avila, K. Ando, and C. D. Ohl, "The fast dynamics of cavitation bubbles within water confined in elastic solids," Soft Matter **10**, 1455–1461 (2014).
[11] O. Vincent, D. A. Sessoms, E. J. Huber, J. Guioth, and A. D. Stroock, "Drying by cavitation and poroelastic relaxations in porous media with macroscopic pores connected by nanoscale throats," Phys. Rev. Lett. **113**(13), 134501 (2014).
[12] O. Vincent, P. Marmottant, P. A. Quinto-Su, and C. D. Ohl, "Birth and growth of cavitation bubbles within water under tension confined in a simple synthetic tree," Phys. Rev. Lett. **108**(18), 184502 (2012).
[13] Q. X. Wang, "Non-spherical bubble dynamics of underwater explosions in a compressible fluid," Phys. Fluids **25**(7), 072104 (2013).
[14] E. Klaseboer and B. C. Khoo, "An oscillating bubble near an elastic material," J. Appl. Phys. **90**, 5808–5818 (2004).
[15] C. K. Turangan, G. P. Ong, E. Klaseboer, and B. C. Khoo, "Experimental and numerical study of transient bubble-elastic membrane interaction," J. Appl. Phys. **100**, 054910 (2006).

[16]E. A. Brujan, K. Nahen, and P. Schmidt, "Dynamics of laser-induced cavitation bubbles near a elastic boundary: Influence of the elastic modulus," J. Fluid Mech. **433**, 283–314 (2001).
[17]G. A. Curtiss, D. M. Leppinen, Q. X. Wang, and J. R. Blake, "Ultrasonic cavitation near a tissue layer," J. Fluid Mech. **730**, 245–272 (2013).
[18]S. J. Lind and T. N. Phillips, "The influence of viscoelasticity on the collapse of cavitation bubbles near a rigid boundary," Theor. Comput. Fluid Dyn. **26**, 245–277 (2012).
[19]S. J. Lind and T. N. Phillips, "The effect of viscoelasticity on the dynamics of gas bubbles near free surfaces," Phys. Fluids **25**(2), 022104 (2013).
[20]M. L. Calvisi, O. Lindau, J. R. Blake, and A. J. Szeri, "Shape stability and violent collapse of microbubbles in acoustic traveling waves," Phys. Fluids **19**(4), 047101 (2007).
[21]S. W. Fong, E. Klaseboer, C. K. Turangan, B. C. Khoo, and K. C. Hung, "Numerical analysis of a gas bubble near biomaterials in an ultrasound field," Ultrasound. Med. Biol. **32**(6), 925–942 (2006).
[22]S. W. Fong, E. Klaseboer, and B. C. Khoo, "Interaction of microbubbles with high intensity pulsed ultrasound," J. Acoust. Soc. Am. **123**(3), 1784–1793 (2008).
[23]Q. X. Wang and J. R. Blake, "Non-spherical bubble dynamics in a compressible liquid. Part 1. Travelling acoustic wave," J. Fluid Mech. **659**, 191–224 (2010).
[24]Q. X. Wang and J. R. Blake, "Non-spherical bubble dynamics in a compressible liquid. Part 2. Acoustic standing wave," J. Fluid Mech. **679**, 559–581 (2011).
[25]Q. X. Wang and K. Manmi, "Microbubble dynamics near a wall subjected to a travelling acoustic wave," Phys. Fluids **24**, 032104 (2014).
[26]Q. X. Wang and K. Manmi, "Numerical modelling of the 3D dynamics of ultrasound contrast agent microbubbles using the BIM," Phys. Fluids **27**, 022104 (2015).
[27]S. P. Wang, A. M. Zhang, Y. L. Liu, and D. R. Zeng, "Numerical simulation of bubble dynamics in an elastic vessel," Eur. Phys. J. **36**(10), 119 (2013).
[28]W. Lauterborn and T. Kurz, "Physics of bubble oscillations," Rep. Prog. Phys. **73**, 106501 (2010).
[29]C. E. Brennen, *Cavitation and Bubble Dynamics*, Oxford Engineering Science Series Vol. 44 (Oxford University Press, New York, Oxford, 1995).
[30]D. D. Joseph and J. Wang, "The dissipation approximation and viscous potential flow," J. Fluid Mech. **505**, 365–377 (2004).
[31]E. Klaseboer, R. Manica, D. Y. C. Chan, and B. C. Khoo, "BEM simulations of potential flow with viscous effects as applied to a rising bubble," Eng. Anal. Boundary Elem. **35**, 489–494 (2011).
[32]S. Li, Y. B. Li, and A. M. Zhang, "Numerical analysis of the bubble jet impact on a rigid wall," Appl. Ocean Res. **50**, 227–236 (2015).
[33]A. M. Zhang and B. Y. Ni, "Three-dimensional boundary integral simulations of motion and deformation of bubbles with viscous effects," Comput. Fluids **92**, 22–33 (2014).
[34]K. Manmi and Q. X. Wang, "Acoustic microbubble dynamics with viscous effects," Ultrason. Sonochem. **36**, 427–436 (2017).
[35]M. J. Walters and T. N. Phillips, "A non-singular boundary element method for modelling bubble dynamics in viscoelastic fluids," J. Non-Newtonian Fluid Mech. **235**(Suppl. C), 109–124 (2016).
[36]C.-T. Hsiao, A. Jayaprakash, A. Kapahi, J.-K. Choi, and G. L. Chahine, "Modelling of material pitting from cavitation bubble collapse," J. Fluid Mech. **755**, 142–175 (2014).
[37]J. R. Blake and D. C. Gibson, "Growth and collapse of a vapour cavity near a free surface," J. Fluid Mech. **111**, 123–140 (1981).
[38]Q. X. Wang, K. S. Yeo, B. C. Khoo, and K. Y. Lam, "Strong interaction between a buoyancy bubble and a free surface," Theor. Comput. Fluid Dyn. **8**, 73–88 (1996).
[39]Q. X. Wang, K. S. Yeo, B. C. Khoo, and K. Y. Lam, "Nonlinear interaction between gas bubble and free surface," Comput. Fluids **25**(7), 607–628 (1996).
[40]Q. X. Wang, "Local energy of a bubble system and its loss due to acoustic radiation," J. Fluid Mech. **797**, 201–230 (2016).
[41]Q. Wang, "Multi-oscillations of a bubble in a compressible liquid near a rigid boundary," J. Fluid Mech. **745**(4), 509–536 (2014).
[42]D. Fuster and F. Montel, "Mass transfer effects on linear wave propagation in diluted bubbly liquids," J. Fluid Mech. **779**, 598–621 (2015).
[43]I. Akhatov, O. Lindau, A. Topolnikov, R. Mettin, N. Vakhitova, and W. Lauterborn, "Collapse and rebound of a laser-induced cavitation bubble," Phys. Fluids **13**(10), 2805–2819 (2001).
[44]A. J. Szeri, B. D. Storey, A. Pearson, and J. R. Blake, "Heat and mass transfer during the violent collapse of nonspherical bubbles," Phys. Fluids **15**(9), 2576–2586 (2003).
[45]Q. X. Wang, K. S. Yeo, B. C. Khoo, and K. Y. Lam, "Vortex ring modelling for toroidal bubbles," Theor. Comput. Fluid Dyn. **19**(5), 303–317 (2005).
[46]Y. L. Liu, Q. X. Wang, S. P. Wang, and A. M. Zhang, "The motion of a 3D toroidal bubble and its interaction with a free surface near an inclined boundary," Phys. Fluids **28**, 122101 (2016).
[47]A. M. Zhang and Y. L. Liu, "Improved three-dimensional bubble dynamics model based on boundary element method," J. Comput. Phys. **294**(1), 208–223 (2015).
[48]A. M. Zhang, S. Li, and J. Cui, "Study on splitting of a toroidal bubble near a rigid boundary," Phys. Fluids **27**, 062102 (2015).
[49]Y. L. Liu, S. P. Wang, and A. M. Zhang, "Interaction between bubble and air-backed plate with circular hole," Phys. Fluids **28**, 062105 (2016).
[50]N. N. Liu, P. Cui, S. F. Ren, and A. M. Zhang, "Study on the interactions between two identical oscillation bubbles and a free surface in a tank," Phys. Fluids **29**, 052104 (2017).
[51]M. S. Plesset and A. Prosperetti, "Bubble dynamics and cavitation," Annu. Rev. Fluid Mech. **9**, 145–185 (1977).
[52]J. R. Blake and D. C. Gibson, "Cavitation bubbles near boundaries," Annu. Rev. Fluid Mech. **19**, 99–123 (1987).
[53]P. Cui, Q. X. Wang, S. P. Wang, and A. M. Zhang, "Experimental study on interaction and coalescence of synchronized multiple bubbles," Phys. Fluids **28**(1), 012103 (2016).
[54]S. Zhang, S. P. Wang, and A. M. Zhang, "Experimental study on the interaction between bubble and free surface using a high-voltage spark generator," Phys. Fluids **28**(3), 032109 (2016).
[55]N. Hosseinkhah, H. Chen, T. J. Matula, P. N. Burns, and K. Hynynen, "Mechanisms of microbubble-vessel interactions and induced stresses: A numerical study," J. Acoust. Soc. Am. **134**(3), 1875–1885 (2013).
[56]H. Chen, "Ultra-high speed optical imaging of ultrasound-activated microbubbles in mesenteric microvessels," Ph.D. thesis (University of Washington, 2011).
[57]T. G. Leighton, *The Acoustic Bubble* (Academic Press, 1994).